INTERNATIONAL JOURNAL OF
Minerals, Metallurgy and Materials

*Volume 31, Number 4, April 2024*
*Page 725*

Research Article https://doi.org/10.1007/s12613-023-2772-9

# Preheating-assisted solid-state friction stir repair of Al–Mg–Si alloy plate at different rotational speeds

*Hui Wang*[1)], *Yidi Li*[1)], *Ming Zhang*[1)], *Wei Gong*[1)], *Ruilin Lai*[2),✉], *and Yunping Li*[1),✉]

1) State Key Laboratory of Powder Metallurgy, Central South University, Changsha 410083, China
2) Research Institute of Light Alloy, Central South University, Changsha 410083, China
(Received: 31 July 2023; revised: 30 October 2023; accepted: 17 November 2023)

**Abstract:** Additive friction stir deposition (AFSD) is a novel structural repair and manufacturing technology has become a research hotspot at home and abroad in the past five years. In this work, the microstructural evolution and mechanical performance of the Al–Mg–Si alloy plate repaired by the preheating-assisted AFSD process were investigated. To evaluate the tool rotation speed and substrate preheating for repair quality, the AFSD technique was used to additively repair 5 mm depth blind holes on 6061 aluminum alloy substrates. The results showed that preheat-assisted AFSD repair significantly improved joint bonding and joint strength compared to the control non-preheat substrate condition. Moreover, increasing rotation speed was also beneficial to improve the metallurgical bonding of the interface and avoid volume defects. Under preheating conditions, the UTS and elongation were positively correlated with rotation speed. Under the process parameters of preheated substrate and tool rotation speed of 1000 r/min, defect-free specimens could be obtained accompanied by tensile fracture occurring in the substrate rather than the repaired zone. The UTS and elongation reached the maximum values of 164.2 MPa and 13.4%, which are equivalent to 99.4% and 140% of the heated substrate, respectively.

**Keywords:** additive friction stir deposition; structural repair; tool rotation speed; Al alloy

## 1. Introduction

As heat-treatable strengthening Al alloys, 6xxx aluminum alloys demonstrate low density, high strength, and high corrosion resistance [1–4]. They are widely used in various fields such as automobiles, high-speed railways, and sports facilities [5–8]. However, components made of 6xxx Al alloys, such as railway body and aircraft fuselage frames, are prone to corrosion, wear, and cutting [9–10]. In such cases, structural repair is an economical and effective approach to renewing the loading capability of components compared to replacing them with new ones.

Conventional repair methods of Al components are generally based on fusion welding technology, like tungsten inert gas (TIG) welding technology. For example，6061 Al alloy was repaired via melting welding wires with a TIG torch and pushing the droplets into a molten pool with high-purity Ar gas [11]. The results suggested that ER 5356 welding wire is more suitable to improve repair quality. The maximum tensile strength welding coefficient is 70.3% although there were a few micro-cracks in the welding zone. Naing and Muangjunburee [12] used metal inert gas (MIG) welding technology to repair 6082 Al alloy and some minor pores were observed in the fusion zone. In fusion-based welding technology, molten Mg in welding wire, characterized by a rapid solidification rate, would hinder the release of hydrogen and enable the accumulation of hydrogen, resulting in pores and micro-cracks [12], which are harmful to the mechanical properties of components.

Additive friction stir deposition (AFSD) is a type of solid-state additive manufacturing technology that can effectively overcome solidification defects [13]. One of the key features of the AFSD process is that the peak temperature of the material is only 0.6–0.9 times of melting point, which can effectively avoid the defects, such as shrinkage and thermal cracking [14–17]. During the AFSD process, a consumable solid rod is rapidly rotated by a hollow non-consumable tool and pushed out through a tool by an upper axial force. As a result, the top end surface of the solid rod becomes softened ascribed to the frictional heat generated between the solid rod and substrate, which leads to severe plastic deformation [18–19].

AFSD is capable of producing both single and multilayer deposits with high-quality interfaces and without anisotropic microstructures, while also significantly refines the microstructure of cast aluminum alloys from 200 to 5 μm. The co-deformation of deposited materials and substrate at high temperatures results in strong metallurgical bonding, and subsequent layers are deposited on the substrate surface through the in-plane motion of the tool head [20]. AFSD can produce not only single-layer deposits with excellent mechanical properties, but also multilayer deposits with high-quality in-

✉ Corresponding authors: Ruilin Lai Email: lairuilin@csu.edu.cn; Yunping Li lyping@csu.edu.cn

terfaces and avoid anisotropic microstructures [21–23]. It is worth noting that AFSD can significantly refine the microstructure of cast aluminum alloys (2xxx [24–26], 5xxx [17,27–28], 6xxx [29–32], and 7xxx [19,33]) from 200 to about 5 μm. Compared the deposition rates with those of other additive manufacturing technologies for aluminum alloys, such as laser powder bed fusion technology (2.52 $cm^3$/h) and directed energy deposition (4.06 $cm^3$/h), AFSD (1020 $cm^3$/h) is much more efficient [34]. Moreover, AFSD is not only used for additive manufacturing aluminum alloys but also widely used for other alloys such as magnesium alloys [35–36], copper alloys [37], titanium alloys [18], nickel alloys [38], steel [39]. AFSD is not only used in additive manufacturing, but also in structural repair. As a novel approach for structural repair, there are a few studies on structural repair using AFSD. Griffiths *et al.* [40] repaired through-hole and wide groove on 7075 Al alloy plate by AFSD process. The results indicated, however, that only ~1.6–3.3 mm above the through-hole is well repaired, where metallurgical bonding is formed. Avery *et al.* [41] also repaired 7075 Al alloy grooves by AFSD. The measured mean grain size is about 5 μm, showing equiaxed fine grains due to continuous dynamic recrystallization (CDRX). Martin *et al.* [42] utilized AFSD to repair long grooves with different geometries on 6061 Al alloys. The results indicated that the groove shape had little effect on repair quality, and the effective repair depth was 2.3–2.6 mm. The poor metallurgical bonding can be ascribed to insufficient plastic flow of materials due to low shear force. From the aforementioned results, it is clear that enhancing the material's flowability is the key point to improving repair quality. Since the frictional heat generated is strongly dependent on but limited by the AFSD process, preheating should be an effective strategy to additionally increase the flowability of materials and therefore to improve the repair quality. However, the effect of preheating on repair quality by AFSD has not been studied.

Despite the above efforts, there are still many problems to be solved in the AFSD repair, such as insufficient material flow at the bottom of the hole and poor metallurgical bonding in the interface. Hence, a simplified AFSD method for blind hole repair was introduced in this study. To improve the bonding at the bottom of the hole, the feedstock rod was placed directly in the hole while rotating and feeding downwards, omitting the lateral tool movement process. Moreover, to improve the materials flow in the hole bottom, preheating in the substrate is performed for the first time. Subsequently, the microstructure evolution and mechanical properties of the Al–Mg–Si alloy plate repaired at different rotational speeds and preheating condition were investigated, with the aim of understanding the relationship between the repaired quality and the heat input. The purpose was to explore the potential benefits and restrictions of AFSD as a solid-state additive repair for Al–Mg–Si alloys.

## 2. Experimental

The used substrate was commercial 6061 Al–Mg–Si alloy, and the feedstock rods were cut from the substrate by wire-cut electrical discharge machining. The chemical composition of the alloy determined by an inductively coupled plasma optical emission spectrometer (ICP-OES, Spectro Blue II, Germany) is shown in Table 1. A typical laminated structure embedded with bright partials was introduced in Al–Mg–Si alloy with an extended direction along the rolling direction (RD). The bright particles are identified as $Al_6$(Fe,Mn,Cr) phases, which was well reported in Refs. [43−44]. Feedstock rods of 7 mm × 7 mm × 300 mm and rolling plates of 200 mm × 260 mm × 10 mm were used for repair. ϕ12 mm inverted-conical blind holes with a depth of 5 mm were drilled into the plate by a tungsten steel drill. All experiments were performed using a self-built AFSD machine. The diameter of the rotation tool is 35 mm and there are four protrusions of 1.5 mm in height on the surface.

Fig. 1 shows the schematic diagram for simplified AFSD repair. The main parameters in the AFSD process are tool rotation speed $\omega$ (revolutions per minute, r/min) and feedstock rod feed speed F (mm/min). Before experiment, the substrate surface was ground with SiC abrasive paper to remove the oxide film and rolling oil on the surface, and cleaned with alcohol after grinding was completed. Then preheating to 270°C was performed on the substrate. The substrate was re-

**Table 1. Chemical composition of the 6061-T6 aluminum alloy** wt%

| Si | Fe | Cu | Mn | Mg | Cr | Zn | Al |
|---|---|---|---|---|---|---|---|
| 0.60 | 0.54 | 0.26 | 0.12 | 1.03 | 0.15 | 0.08 | Bal. |

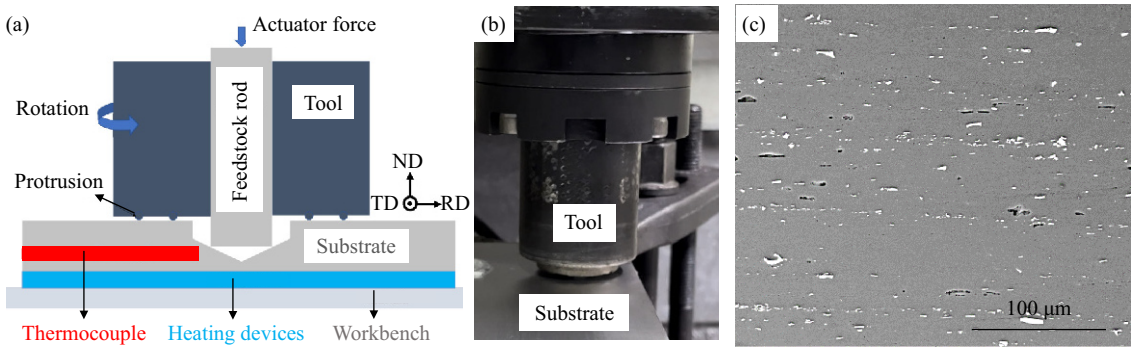


**Fig. 1. (a) Schematic diagram of AFSD repair, (b) photograph of the AFSD repair process, and (c) SEM image under BSE mode of AA 6061-T6 base material.**

paired at a constant feed speed of 10 mm/min and four tool rotation speeds: 400, 600, 800, and 1000 r/min, resulting in specimens denoted by S400, S600, S800, and S1000, respectively. For comparison, another substrate was repaired at 1000 r/min without preheating and the specimen obtained is denoted by S1000-Np. Temperature history during the repair process was monitored by a k-type thermocouple embedded in the substrate, which is under the blind hole. The schematic diagram of the location of the thermocouple is also shown in Fig. 1.

Specimens for microstructure analysis were cut in the plane between the rolling direction (RD) and normal direction (ND) of the plate across the repaired hole. The microstructural observation was performed using optical microscopy (OM) and electron backscattered diffraction (EBSD). For OM observation, the specimen was ground with SiC abrasive paper followed by polishing in oxide polishing suspension (OPS) and etching in Keller's solution. Before EBSD, electro-polishing in a solution of 10vol% perchloric acid ($HClO_4$)–ethyl alcohol ($C_2H_5OH$) at 20 V and −30°C for 20 s was performed. EBSD was conducted using a field emission-gun scanning electron microscope (FESEM, FEI Quanta 650, USA) equipped with an Oxford Instruments Aztec HKL detector with a step size of 0.35 μm. EBSD analysis was performed using commercial HKL channel 5 software. A limited misorientation cut-off of 2° was employed. With discrimination between low-angle grain boundaries (LAGBs) and high-angle grain boundaries (HAGBs), a 15° criterion was adopted [45].

Vickers hardness of cross-section was measured by a microhardness tester (200HV-5, China) at a load of 3 Nfor 10 s. A schematic illustration for the hardness test is shown in Fig. 2. Hardness along six lines was measured at an interval of 1 mm on the cross-section. The interval between two adjacent indentations was 1 mm. The tensile specimen was cut into a dog-bone shape along RD with a gauge section of 64 mm and width of 10 mm according to GB/T 228.1—2021, while the repaired hole was located at the center of the gauge section. Tensile tests were performed on a tensile testing machine (UTM 5105, China) at a constant crosshead speed of 1 mm/min.

## 3. Results

### 3.1. Temperature evolution

Fig. 3 shows the temperature history near the blind hole during repair for different repair conditions. For the preheated specimen, the temperature of the substrate is about 250°C before repair, which is a little lower than the pre-set value (270°C), possibly due to the mass heat loss from the upper surface. With the progress of repair, the temperature near the hole increased significantly in all conditions. From the results in Fig. 3, the peak temperature increases gradually from 360.8 to 468.3°C accordingly with rotation speed increased from 400 to 1000 r/min. It facilitates the improvement of the flow of the deposited material, making it easier to fill the entire blind hole. In contrast, the peak temperature of the S1000-Np specimen is 383.9°C, which is much lower than the S1000 specimen (468.3°C). The lack of preheating of the substrate resulted in a lower overall heat input. The increase in temperature values due to the increase in rotation speed and the introduction of preheating may change the microstructure and mechanical properties of the joints, which will be discussed in the following sections.

### 3.2. Microstructure

The top surface appearance of the specimen after repairing at 4 rotation speeds is shown in Fig. 4, where the orientation between the tensile specimen and the blind hole is schematically drawn. From the surface, all the holes were well repaired without apparent defects. The blind hole (red dashed circle) has been filled by deposited material. During the repair process, the feedstock continues downward until the deposited material spills over the tool shoulder. Flash edges were observed on the surface of all specimens (yellow arrows).

The cross-sectional morphologies of the blind holes at different rotation speeds is revealed in Fig. 5, which is comprised of multiple optical micrographs stitched together. The figures in Fig. 5(a)–(e) shows that all blind holes are successfully filled with deposited materials. However, there are differences in the details of different interfaces. At 400 r/min, the interface between the deposited material and blind hole (red dashed line in Fig. 5(a)) is straight and almost coincides with the raw blind hole wall (white dashed line in Fig. 5(a)). As the rotation speed increases to 600 and 800 r/min, the in-

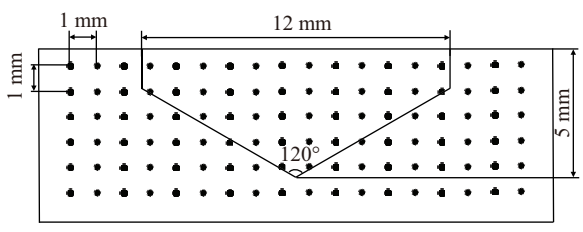


**Fig. 2. Original dimension of vertical section of hole and schematic illustration of the repaired specimen for microhardness tests.**

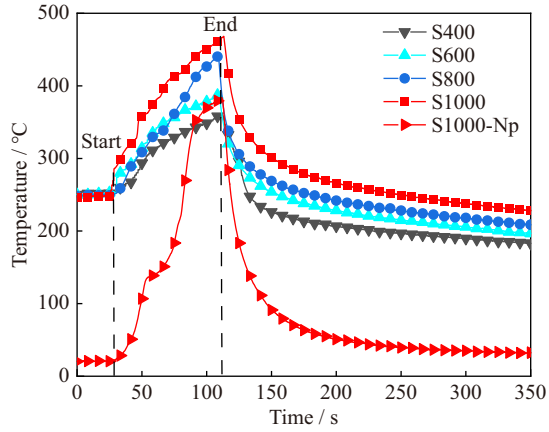


**Fig. 3. Temperature history of repaired process at different rotation speeds.**

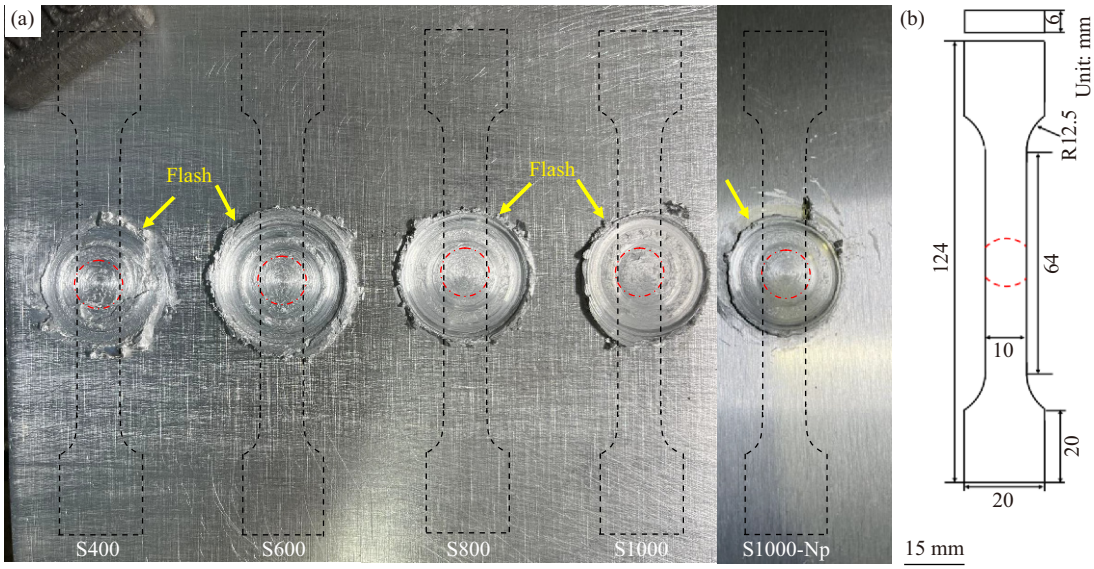


**Fig. 4. (a) Surface features of the repaired samples at different rotational speeds and schematic diagram of sampling position for tensile samples. (b) Dimensional figure of the tensile specimen.**

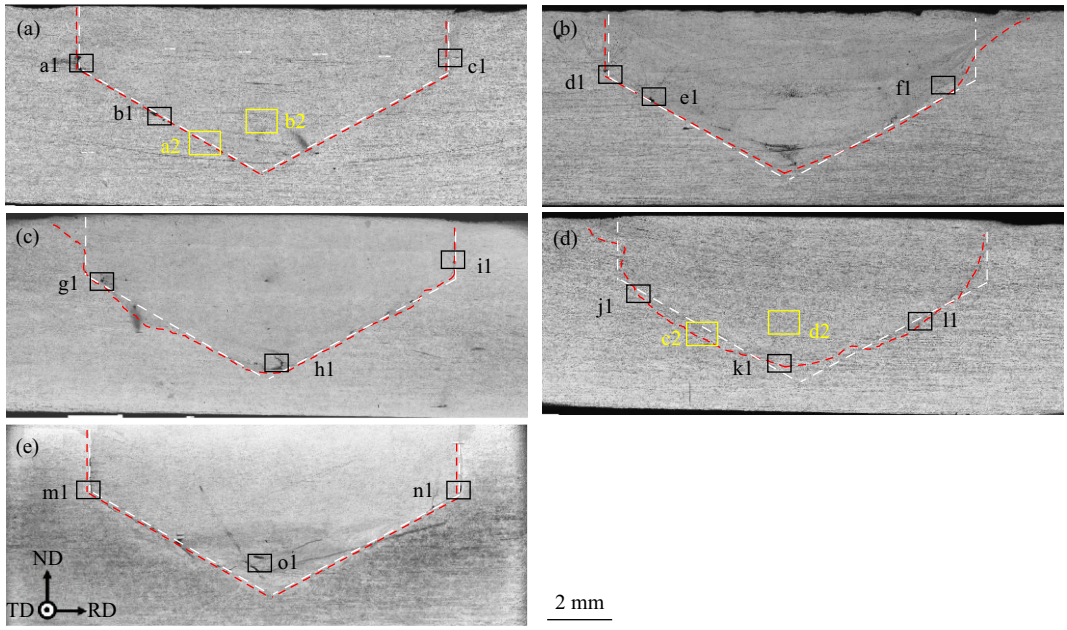


**Fig. 5. Cross-sectional morphologies of repaired specimens at different tool rotation speeds: (a) 400 r/min, (b) 600 r/min, (c) 800 r/min, (d) 1000 r/min, and (e) 1000 r/min, the non-preheated specimen.**

terface becomes sinuous, suggesting a higher bonding quality in the interface. At 1000 r/min, a defect-free joint is observed as shown in Fig. 5(d). The original interface (white dashed line in Fig. 5(d)) is well disrupted by the deposited material and then the new curved interface (red dashed line in Fig. 5(d)) is reconstructed. For the non-preheated specimen after repairing at 1000 r/min (Fig. 5(e)), a straight interface between the deposited material and blind hole wall is observed. This suggests the significant influence of preheating on repair quality during AFSD.

A further inspection of the interface zones in Fig. 5 is displayed in Fig. 6. Under higher magnification, volume vacancies and kissing bonds can be observed at 400-600 r/min. Such kissing defects and volume vacancies are still observed at the interface until the rotation speed of 800 r/min (Fig. 6(g)–(i)), indicating that material flow is still inadequate. At 1000 r/min as shown in Fig. 6(j)–(l), no above-mentioned cavity defects were observed. At higher speeds, more local strain inside the blind hole results in lower flow stress in the material. This leads to better filling of the blind holes by the deposited material and avoids the formation of cavity. The good metallurgical bonding at the interface (red dashed line in Fig. 6(j)–(l)) can be attributed to the increased frictional heat input at higher speeds. In contrast, for the non-preheated specimen shows volume defects and weak metallurgical bonding at the interface as shown in Fig. 6(m)–(o). Thus, preheating during the repair process can significantly avoid the formation of volumetric defects and improve metallurgical bonding.

Given the information about the S1000 specimen provided

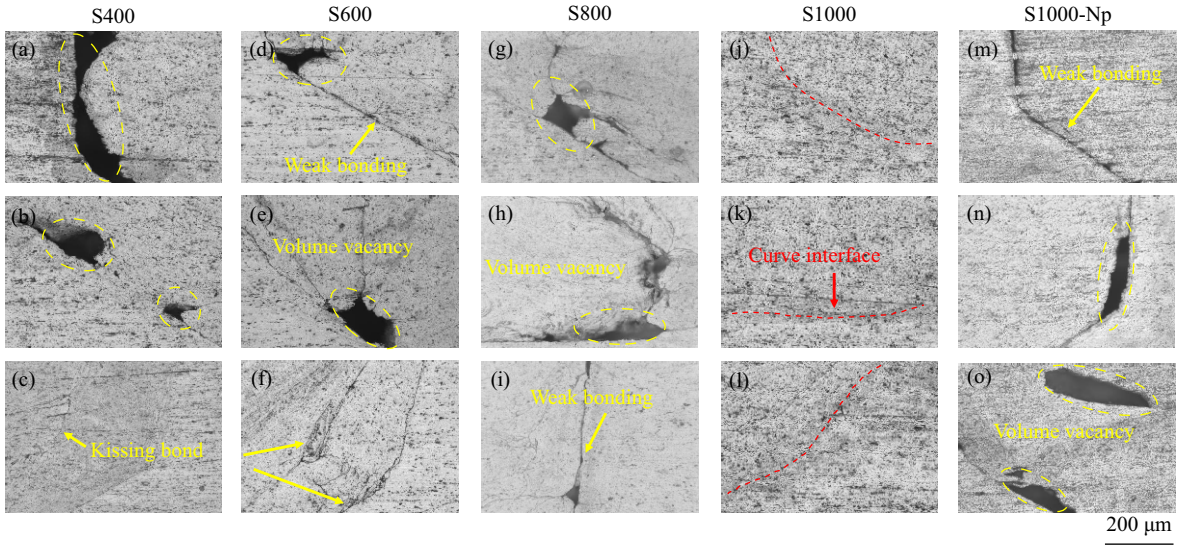


**Fig. 6. (a–o) Marked local magnified graphs corresponding to the black boxes a1–o1 in Fig. 5.**

by OM is limited, further high-resolution characterization like SEM is still necessary. Fig. 7 presents the SEM images of the S1000 specimen, specifically focusing on the interface which is indicated by the white dashed line. The substrate displayed distinct laminated precipitates, which were a result of the rolling process. However, the repaired zone exhibited a more diffuse distribution of precipitated phase characteristics after the repair. Based on the findings in Fig. 7, it can be concluded that the S1000 specimen achieved a favorable metallurgical bonding between the deposited material and the substrate at both the bottom and top positions of the blind holes. No aggregation of precipitates or formation of intermetallic compounds was observed at the interface.

Microstructural characterization by using EBSD was performed for the preheated specimens at 400 and 1000 r/min, which represent the lowest and highest rotation speed. EBSD mapping at both the interface zone and the repaired zone was made at regions a2 and c2, b2 and d2, respectively, as noted by yellow wireframe in Fig. 5. Fig. 8 shows the EBSD image quality figures and inverse pole figures of the interface zone. As shown in Fig. 8, typical elongated grains are observed on the left side of the interface for the rolled substrate side. The repaired zones present significant grain refinement, which is characteristic of the AFSD process. During AFSD, the initial grain boundaries consist of low angle grain boundaries (LAGBs) with local misorientation angles, which change and rotate due to the mechanical stirring action of the feedstock rod, and their misorientation angles increase. As a result, the LAGBs are transformed into high angle grain boundaries (HAGBs), and fine grains are formed in the microstructure. In addition, high deformation temperatures or low strain rates play a critical role in the homogeneity of the recrystallized microstructure. Fig. 9 shows the EBSD analysis results of the inner repaired zone at 400 and 1000 r/min. It is clear from Fig. 9(a) and (d) that the grains in the repaired zone increase with increasing speed. The mean grain size of the repaired zone at 400 and 1000 r/min is 2.46 and 2.96 μm, respectively. The measured LAGBs fraction in the repaired zones is 10.3%

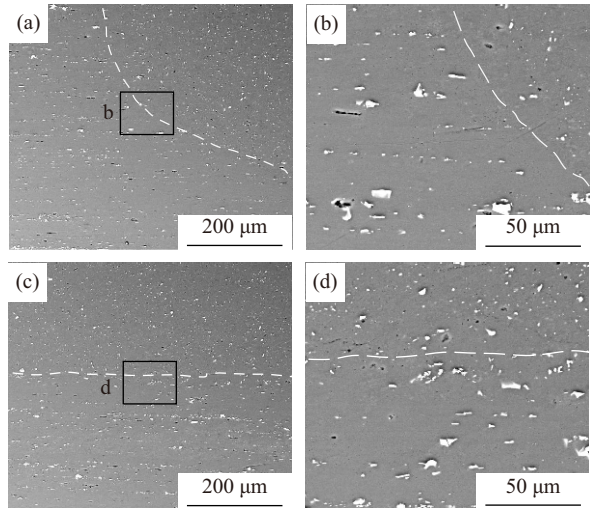


**Fig. 7. SEM images of the S1000 sample in BSE mode at the top interface (a–b) and the bottom interface (c–d). (a) and (c) are taken from the black boxes j1 and k1 in Fig. 5(d), respectively.**

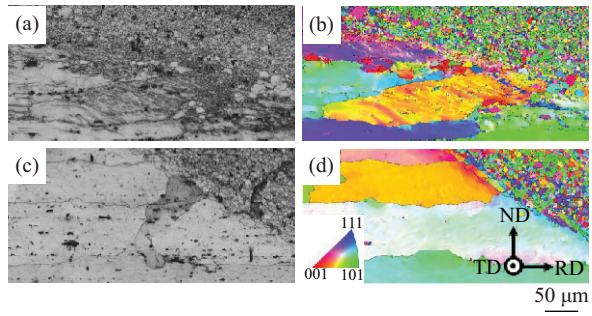


**Fig. 8. EBSD image quality figures and inverse pole figures of interface zone: (a, b) 400 r/min and (c, d) 1000 r/min.**

and 20.6% at 400 and 1000 r/min, respectively. During the AFSD process, the dislocation density and fraction of LAGBs increase with increasing strain. At the same time, the heat input also has a considerable effect on the proportion of LAGBs: owing to high thermal exposure, the majority of formed sub-structures and dislocations are consumed and

form LAGBs [2]. This type of microstructure is often seen in AFSD of Al alloys, which is commonly ascribed to the development of CDRX [46–48].

### 3.3. Mechanical performance

Cross-sectional microhardness distributions of repaired specimens with preheating condition at different rotation speeds are shown in Fig. 10, where the dashed lines represent the raw position of the blind hole. The maximum and minimum microhardneses are HV 66.5 and HV 40.0, respectively, suggesting the obvious softening compared to the raw feedstock (approximately HV 115.5). This is consistent with the results of other AFSD studies, where the microhardness of the deposits is significantly reduced due to the dissolution of the precipitates [49–50]. There is no significant difference in the microhardness of the repaired zone at different rotation speeds. For the S400 specimen, the minimum microhardness corresponds to the volume defects.

Fig. 11 shows the engineering stress–strain curves and a summary of mechanical properties at different rotation speeds. The ultimate tensile strength (UTS) and fractured elongation of the raw substrate after repair are 165.2 MPa and 9.6%, respectively. Because of the dissolution and coarsening of the precipitated phase, the UTS is significantly decreased compared to the raw substrate. The S1000-Np specimen demonstrated the lowest mechanical properties. The UTS and elongation were 73.7 MPa and 3.0%, respectively. For the preheated specimen, with increasing rotation speed, both UTS and elongation increase gradually. At 400 r/min, the UTS and elongation of the specimen was 92.5 MPa and 3.6% respectively, which was also higher than that of the non-preheated specimen at 1000 r/min. At a rotation speed of

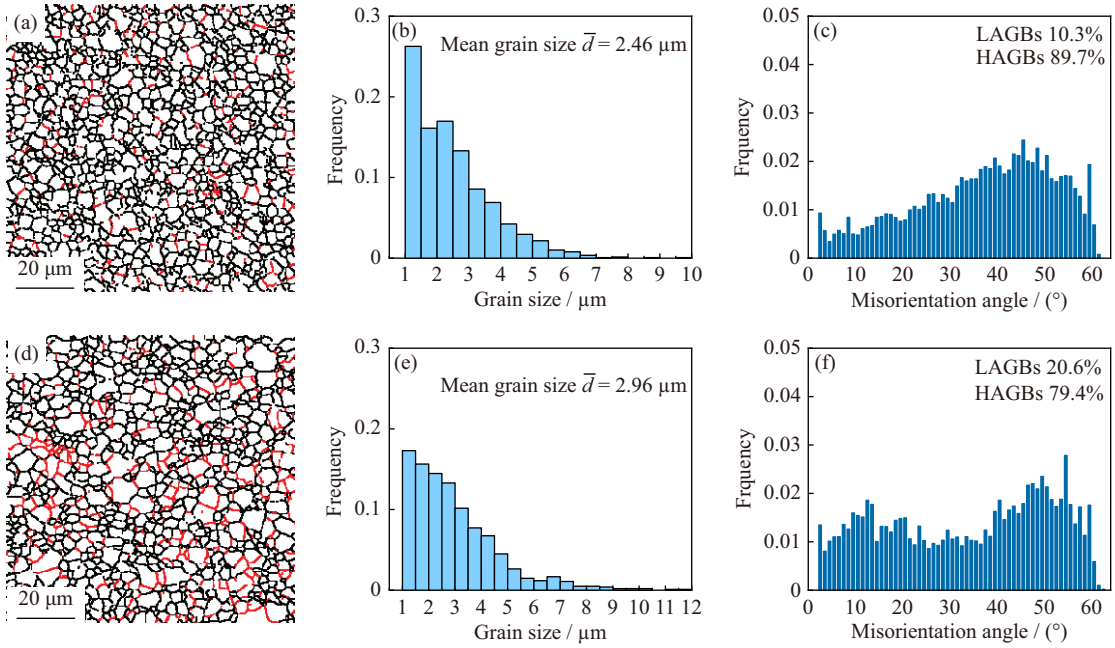


**Fig. 9. EBSD analysis results of the inner repaired zone: (a–c) 400 r/min and (d–f) 1000 r/min; (a, d) grain-boundary maps, (b, e) grain size distribution, and (c, f) misorientation angle distribution.**

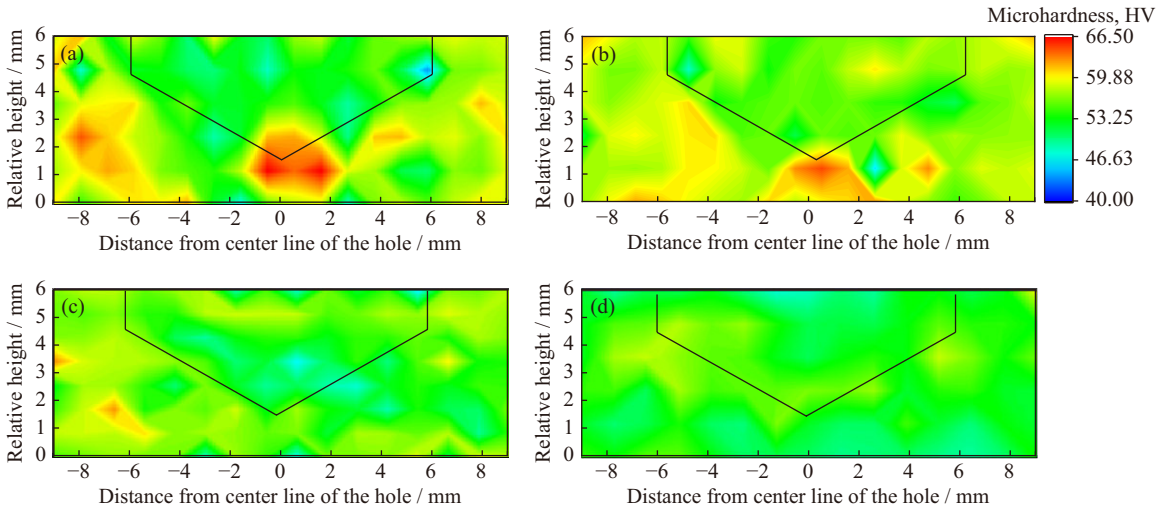


**Fig. 10. Cross-sectional hardness distribution maps of repaired specimens at different rotation speeds: (a) S400, (b) S600, (c) S800, and (d) S1000.**

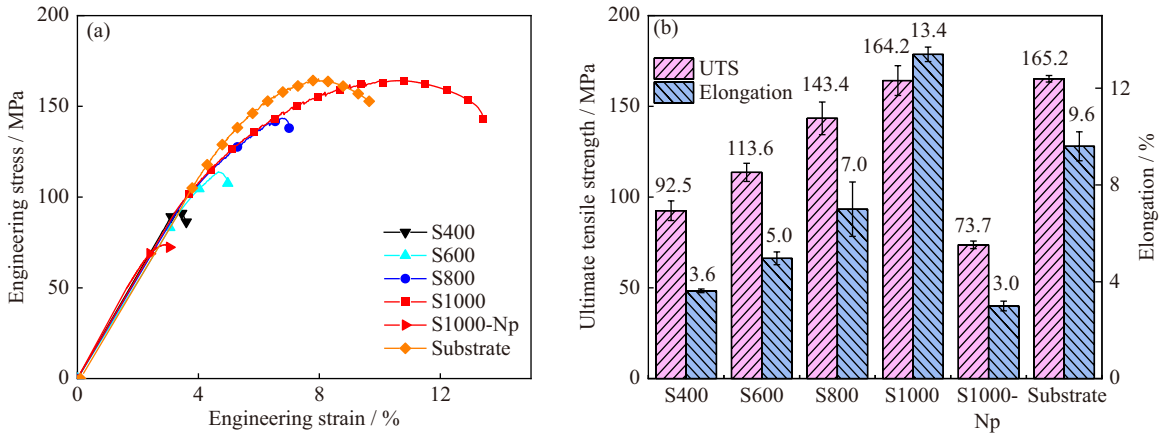


**Fig. 11. (a) Engineering stress–strain curves of Al–Mg–Si alloys under different conditions and (b) summary mechanical properties.**

1000 r/min, interfacial defects are eliminated due to increased frictional heat input and enhanced material flow behavior. The UTS of the repaired joint is 164.2 MPa and the elongation of the specimen is 13.4%. The longer elongation could be ascribed to the refined grains in the repaired zone. Microstructures with finer grains provide higher ductility than microstructures with coarse grains, which can efficiently coordinate plastic deformation and hinder the initiation of microcracks [51].

### 3.4. Fractography

Fig. 12 presents the macroscopic profiles of repaired specimens after tensile tests. For the specimens repaired at lower rotation speeds or without preheating, the fracture takes place dominantly at the interface as indicated by the black dashed line. On the contrary, the fracture of the S1000 specimen occurred far away from the blind hole wall, implying higher bonding stress between the deposited materials and substrate than the strength of the substrate. Fig. 13 shows the lateral features of the stretched sample that has been broken, which can reflect the location of the fracture. The S1000 specimen demonstrates different fracture features compared to the others. The interface remains intact, and fracture occurs in the substrate.

Fig. 14 shows the cross-sectional SEM morphologies of fractured specimens under different repair conditions. The local magnified figures of the squared areas are exhibited in Fig. 14 (f)–(j), accordingly. As arrowed in Fig. 14(a) and (e),

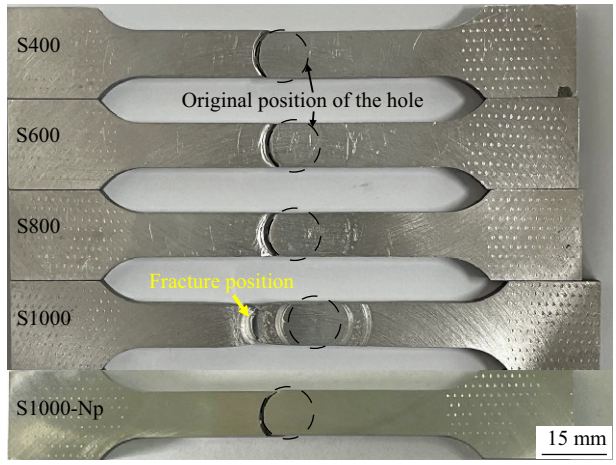


**Fig. 12. Fracture features of the tensile specimens at different tool rotation speeds.**

the interface between the deposited material and the substrate can be clearly seen, which is caused by volume defects. During the stretching process, stress concentration occurs at volume defects or kissing bonding, and cracks initiate preferentially. The crack propagates along the bonding interface leading to eventual fracture. Furthermore, the fracture surface is smooth without severe deformation and no metallurgical bonding is observed. For both the S600 specimen and the S800 specimen, although the fracture occurred at the hole wall, metallurgical bonding is formed at the bottom of the blind hole. As shown in the white wireframe in Fig. 14(b)–

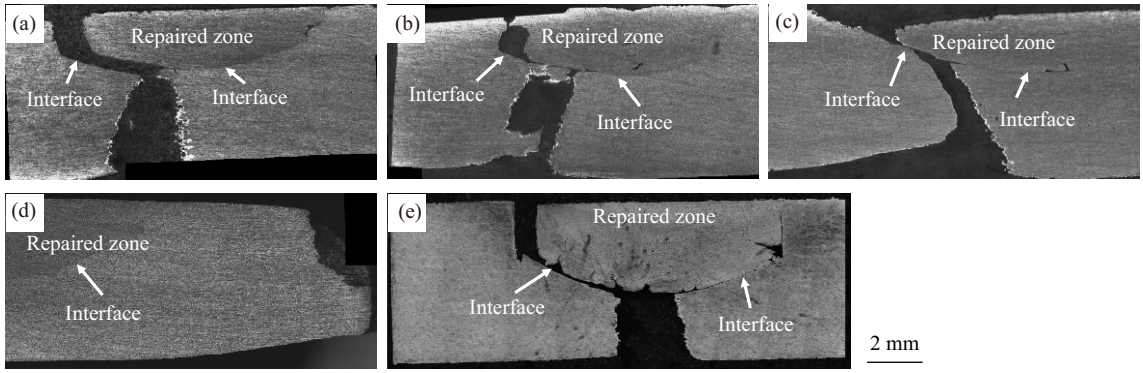


**Fig. 13. Lateral fracture features of tensile specimens at different tool rotation speeds: (a) S400, (b) S600, (c) S800, (d) S1000, and (e) S1000-Np.**

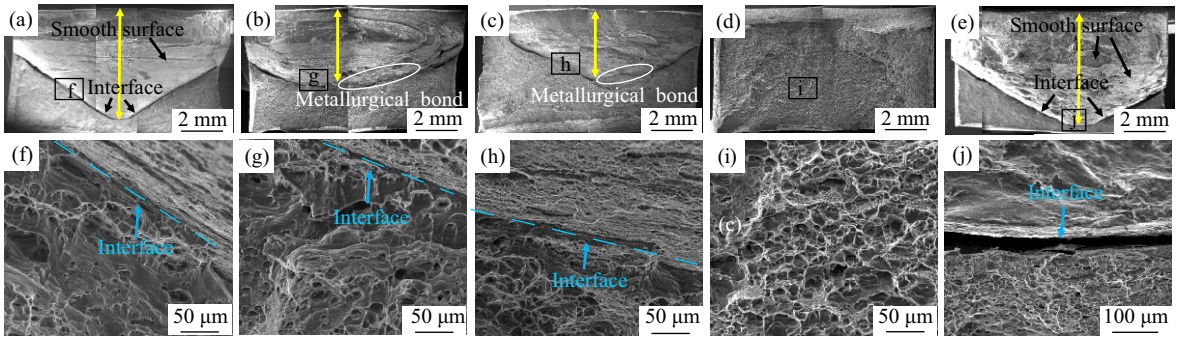


**Fig. 14. SEM micrographs showing fracture surface at different tool rotation speeds: (a, f) S400, (b, g) S600, (c, h) S800, (d, i) S1000, and (e, j) S1000-Np.**

(c), the deposited material is bonded to the substrate and does not become the origin of crack generation during the tensile process. However, the fracture morphology of the S1000 specimen shows completely different characteristics, as shown in Fig. 14(d). The interface is not observed because it fractures entirely at the substrate. The fracture of the specimen showed obvious necking and homogeneous dimples on the surface, indicating large plastic deformation.

According to the fracture morphology, the maximum unrepaired depth (yellow line in the figure) is defined, referring to the longest distance from the upper surface of the blind hole to the position where metallurgical bonding occurs. Fig. 15 shows the statistical results, where the maximum unrepaired depth decreases as the speed increases under preheating conditions. At 400 r/min, the maximum unrepaired depth is 5 mm which is the blind hole depth. As the speed increases from 600 to 800 r/min, the quality of the repair gradually improves and the maximum unrepaired depth decreases from 3.5 to 3.2 mm. At 1000 r/min, the maximum unrepaired depth is 0 mm, indicating the best repair quality. However, as the substrate was not preheated, the maximum unrepaired depth of the specimen changed back to 5 mm at the same rotation speed of 1000 r/min, indicating that preheating had a significant effect on repair quality. The maximum unrepaired depth is also consistent with the results of the tensile test in Fig. 11.

## 4. Discussion

The repair quality of 6061 alloys by AFSD depends strongly on the preheating condition and rotation speed. Significant volume defects are observed in the specimen without preheating even at the highest rotation speed (Fig. 6(m)–(o)). In contrast, specimens with preheating showed higher repair quality at all rotation speeds. Especially, exceptional metallurgical bonding and the defect-free specimen can be obtained at 1000 r/min under preheating condition as shown in Fig. 5(d) and Fig. 6(j)–(l). The SEM images in Fig. 7 demonstrate the same, with a good metallurgical bond formed at the interface between the deposited material and the substrate. The result can be explained from the perspective of heat input, which is mainly due to the preheating and frictional/contact condition. Overall heat input to the substrate can be divided into two parts, $Q_p$ and $Q_f$, which represent accumulated preheated heat input and accumulated frictional heat input, respectively. The total heat input ($Q_t$) can be calculated by the sum of two sections:

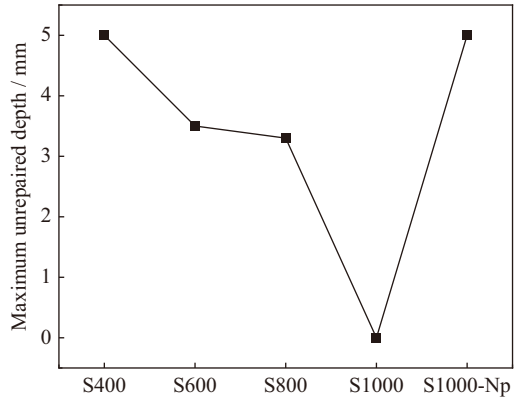


**Fig. 15. Statistical results of the maximum unrepaired depth under different conditions.**

$$Q_t = Q_p + Q_f \quad (1)$$

Since there is no $Q_p$ in the non-preheated specimen, the $Q_t$ of a preheated specimen becomes much higher at a given rotation speed. Assuming that the specific heat capacity ($c$) and mass ($m$) of the plate are constants before and after preheating. $Q_p$ can be calculated by the following formula:

$$Q_p = cm\Delta T \quad (2)$$

where $\Delta T$ is the temperature change of the substrate. The calculated $Q_p$ of the substrate is approximately 603.6 kJ. In addition, after preheating, the substrate becomes softer than the raw feedstock, and plastic deformation around the hole wall is more likely to occur when the feedstock rod is in friction contact with the hole wall. This is demonstrated by the results in Fig. 5(d), a curved interface between deposited material and substrate. Besides, setting the preheating conditions helps the microstructure of the substrate to be more receptive to the joining process and form a metallurgical bond [52]. In general, a reasonable preheating temperature is beneficial in softening the substrate, increasing the overall heat input. In addition, it has been suggested that preheating conditions may help reduce shrinkage stresses and lead to mild cooling rates [53]. In contrast, the specimen without preheating almost maintains volume vacancy is observed at a rotation speed of 1000 r/min. This shows that preheating is a sig-

nificant enhancement to interface bonding.

To further clarify the influence of rotation speed on repair quality, a frictional heat generation model is introduced in this work. As illustrated in Fig. 16, the entire repair process can be classified into two stages, which are characterized by different frictional heat generation patterns. (i) Stage A, heat generated by friction between the feedstock rod and conical hole wall, is defined as $Q_1$. (ii) In stage B, heat is mainly generated by friction between the bottom of the feedstock rod and deposited material, which is defined as $Q_2$. Hence, the total frictional heat input $Q_f$ can be calculated by the following equation:

$$Q_f = Q_1 + Q_2 \tag{3}$$

Eq. (3) is applied on the assumption that: (1) The contact shear stress of the material is uniform; (2) The heat from the plastic deformation of the deposited material was neglected; (3) The square section of the feedstock rod is equivalent to a circle.

All heat is calculated from the following equation [54]:

$$dq = \omega dM = \omega r dF = \omega \tau_c dS = \omega \tau_c r^2 dr d\theta \tag{4}$$

where $dq$ is the friction heat power per unit area, $dM$ is the friction torque per unit area, $dF$ is the friction per unit area, $dS$ is a unit area, $\omega$ is the angular velocity, $\tau_c$ is the contact shear stress, $r$ is the length from arc region to the center, and $dr$ and $d\theta$ are both infinitesimal segments. When the contact friction starts in a sliding state, the contact shear stress ($\tau_c$) can be given by Coulomb's friction law $\tau_c = \tau_f = \mu p$, where $\tau_f$ is the friction stress. When the plastic flow in a sticking state takes place at the interface, $\tau_c = \sigma/\sqrt{3}$. μ is the relative friction coefficient, $p$ is contact pressure, and $\sigma$ is yield strength [55]. Considering the contact state between materials, variable factor $\lambda$ is defined, which represents the percentage of the sticking and sliding state. When the temperature is lower than 50% of the melting point, the variable factor $\lambda$ is 0, and when the temperature reaches 60% of the melting point, $\lambda$ is assumed to be one [56]. Hence, $\tau_c$ can be calculated by the following equation:

$$\tau_c = \lambda \frac{\sigma}{\sqrt{3}} + (1-\lambda)\mu p \tag{5}$$

Heat generation in the 2 stages can obtained independently by an integration [54,55]:

$$Q_1 = \int_0^{2\pi}\int_0^{R_{eq}} h_1 dq_2 = \frac{2}{3}\pi\omega t \tau_c h_1 R_{eq}^3 \left(1 + \cot\frac{\alpha}{2}\right) \tag{6}$$

where $\alpha$ is the blind hole taper angle.

$$Q_2 = \int_0^{2\pi}\int_0^{R_{eq}} h_2 dq_2 = \frac{2}{3}\pi\omega t \tau_c h_2 R_{eq}^3 \tag{7}$$

$$Q_f = \frac{2}{3}\pi\omega t \tau_c \left[h_1 R_{eq}^3 \left(1 + \cot\frac{\alpha}{2}\right) + h_2 R_{eq}^3\right] \tag{8}$$

where $h_1$ and $h_2$ are indicated in Fig. 16(c), respectively.

In this work, since the repair time of different specimens is almost the same, tool diameter, blind hole diameter, and $\alpha$ are geometric constants, and the contact shear stress $\tau_c$ and rotation speed $\omega$ are the variable parameters to frictional heat input. It can be seen from Eq. (8) that the total heat input increases linearly with the product of rotational speed $\omega$ and contact shear stress $\tau_c$. As can be seen from Eq. (5), the shear stress at different rotation speeds is not always the same and is strongly dependent on temperature. To simplify the calculation, the contact shear stress at half of the onset temperature and peak temperature represents the average contact shear stress. The calculated results of frictional heat input and total heat input at different rotational speed are shown in Fig. 17. This is consistent with previous findings on friction-stirred repair, where the frictional heat increases with increasing rotational speed, favoring the formation of a defect-free joint at the interface [57–58]. When the rotation speed increases from 800 to 1000 r/min, the increasing rate of friction heat input becomes lower. This is possibly ascribed to the fact that the contact shear stress of the material becomes very small at high temperatures [56].

Higher heat input by both preheating and higher rotation speed improves the flowability of the deposited material. This can be ascribed to the reduced material flow stress or higher flowability [55]. For these reasons, the variation of mechanical properties in Fig. 11 can be well ascribed to the changed total heat input in Fig. 17. The overall heat input for the S400 specimen is 2500.7 kJ. At 400 r/min, the ultimate

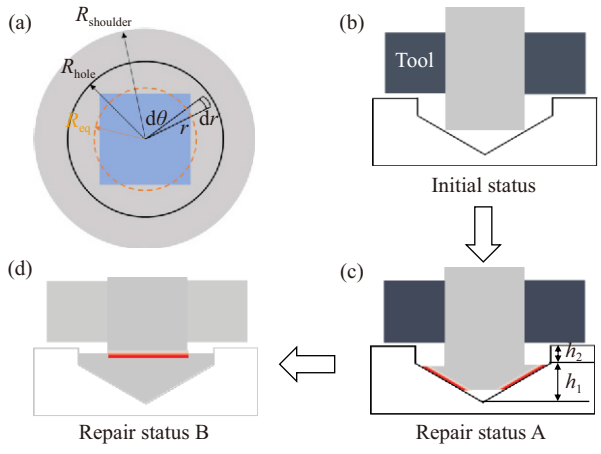


**Fig. 16. Surface infinitesimal segment areas and schematic diagram of different repair stage: (a) cross-section view of tool; (b) initial repair status; (c) repair status A and repair ststus B.**

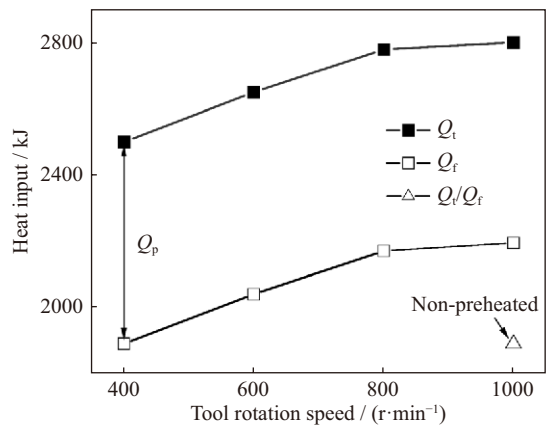


**Fig. 17. Calculated results of heat input of substrate at different rotation speeds.**

tensile strength of the repaired specimen is 92.5 MPa and the repair efficiency is only 56.0%. Repair efficiency increases to 86.8% as the total heat input increases to 2779.2 kJ of 800 r/min. In contrast, the total heat input of the S1000 specimen reaches 2800.7 kJ. The UTS is equivalent to 99.4% of that of the substrate, while the value for the S1000-Np specimen is only 44.6%. When the substrate is not preheated, the friction heat will conduct to the surrounding substrate of the blind hole due to the good thermal conductivity of Al alloy. After preheating, heat accumulates in the substrate, which is more conducive to increasing the local heat input of the blind hole. Comparing these results, it is not hard to find that preheating is a more effective strategy to increase the overall heat input compared to increasing the rotational speed. Nevertheless, to obtain enough heat input, both preheating and high rotation speed are important.

This study provides new ideas for the practical application of AFSD in engineering. Further optimization of process parameters, substrate preheating, and selection of filler materials with similar properties to the substrate can improve material flow and enhance joint strength. The current work achieved better results compared to previous solid-state repair processes. The results of the present work show a maximum repair depth of 5 mm, with the UTS and elongation of the as-repaired joint of 164.2 MPa and 13.4%, respectively. Martin *et al*. [59] repaired Al–Mg–Si alloy plates by AFSD, and the results showed that the maximum UTS of the joint was 149.3 MPa, but the elongation was only 7.0%. Griffiths *et al.* [40] repaired 7075-T6 aluminum alloy by AFSD and showed an effective repair depth of just 1.6 mm. At the bottom of the hole, there was a significant lack of material flow. Ji *et al.* [58] repaired 7N01-T4 aluminum alloy using active-passive filling friction stir technique. The maximum UTS and elongation of the joint were classified as 311.14 MPa and 7.57%. However, the repair efficiency was only 69.9%. 6A01 aluminum alloy was repaired using cold spraying by Zhang *et al.* [60]. The elongation of the repaired joint was 1.2%.

## 5. Conclusions

This work repaired the blind hole of Al–Mg–Si alloy plate by simplified AFSD. To this end, 6061-T6 commercial Al alloy was selected as a target material and AFSD was conducted in a relatively wide range of tool rotation speed from 400 to 1000 r/min. The repair on the non-preheated substrate at 1000 r/min was also conducted. In all cases, the repaired process temperature was monitored, and the evolved microstructure and mechanical properties were investigated. The main conclusions derived from this work were summarized as follows.

(1) The 5 mm depth blind hole was successfully repaired by the simplified AFSD process employing feedstock rods. Microstructural characterization revealed that substantial refined equiaxed grains transformed from elongated grains were observed in the repaired zone.

(2) Preheating substrate can improve significantly the repair quality more than the non-preheating. Cavities or kissing bonding defects are prone to occur in specimens with lower tool rotation speed. Increasing the tool rotation speed is conducive to enhance frictional heat input, improving solid bonding for a defect-free joint.

(3) Under preheating condition, the UTS and elongation are positively correlated with rotation speed. Microhardness does not change significantly with increasing rotation speed. At a rotation speed of 1000 r/min, tensile strength and elongation of the repaired joint reach the maximum values of 164.2 MPa and 13.4%, which are equivalent to 99.4% and 140% of the heated substrate, respectively. Meanwhile, fracture occurs in the substrate rather than in the repaired zone.

Future research should focus on determining the optimal substrate preheating temperature and process parameters, as well as the matching relationship between the two for successful repair. In order to reduce the heat input to the entire substrate, it is best to preheat only the defect site. Heat treatment of the as-repaired joints is a potential strategy to improve the mechanical properties of joints. In addition, other shapes of bulk defects, such as narrow cracks, through holes, and long grooves, can also be experimentally studied to demonstrate the potential of AFSD for solid-state repair. In short, as an emerging additive manufacturing technology, researchers must better understand process fundamentals, material formation mechanisms, and microstructural evolution. This should be necessary to promote the widespread application of AFSD in engineering fields.

## Acknowledgements

This research was financially supported by Science and Technology Major Project of Changsha, China (No. kh2401034), the Fundamental Research Funds for the Central Universities of Central South University (No. CX20230182), and the National Key Research and Development Project of China (No. 2019YFA0709002).

## Conflict of Interest

The authors declare no conflicts of interest.

## References

[1] A. Navabi, M. Vandadi, T. Bond, *et al*., Deformation and cracking phenomena in cold sprayed 6061 Al alloy powders with nanoscale aluminum oxide films, *Mater. Sci. Eng. A*, 841(2022), art. No. 143036.

[2] T. Wang, Y. Zou, X.M. Liu, and K. Matsuda, Special grain boundaries in the nugget zone of friction stir welded AA6061-T6 under various welding parameters, *Mater. Sci. Eng. A*, 671(2016), p. 7.

[3] G.Y. Li, W.M. Jiang, F. Guan, *et al*., mechanical properties and corrosion resistance of A356 aluminum/AZ91D magnesium bimetal prepared by a compound casting combined with a novel Ni–Cu composite interlayer, *J. Mater. Process. Technol.*, 288(2021), art. No. 116874.

[4] G.Y. Li, W.M. Jiang, F. Guan, J.W. Zhu, Y. Yu, and Z.T. Fan, Microstructure evolution, mechanical properties and fracture be-

havior of Al–*x*Si/AZ91D bimetallic composites prepared by a compound casting, *J. Magnesium Alloys*, (2022). DOI: 10.1016/j.jma.2022.08.010

[5] J.C. Williams and E.A. Starke Jr, Progress in structural materials for aerospace systems1, *Acta Mater.*, 51(2003), No. 19, p. 5775.

[6] W.F. Xu, Y.X. Luo, W. Zhang, and M.W. Fu, Comparative study on local and global mechanical properties of bobbin tool and conventional friction stir welded 7085-T7452 aluminum thick plate, *J. Mater. Sci. Technol.*, 34(2018), No. 1, p. 173.

[7] J.L. Zhang, B. Song, Q.S. Wei, D. Bourell, and Y.S. Shi, A review of selective laser melting of aluminum alloys: Processing, microstructure, property and developing trends, *J. Mater. Sci. Technol.*, 35(2019), No. 2, p. 270.

[8] A. Abdollahzadeh, B. Bagheri, A.H. Vaneghi, A. Shamsipur, and S.E. Mirsalehi, Advances in simulation and experimental study on intermetallic formation and thermomechanical evolution of Al–Cu composite with Zn interlayer: Effect of spot pass and shoulder diameter during the pinless friction stir spot welding process, *Proc. Inst. Mech. Eng., Part L: J. Mater.: Des. Appl.*, 237(2022), No. 6, p. 1475.

[9] J.B. Wang, J. Zhang, Y. Zhang, F. Xie, S. Krajnovic, and G.J. Gao, Impact of bogie cavity shapes and operational environment on snow accumulating on the bogies of high-speed trains, *J. Wind Eng. Ind. Aerodyn.*, 176(2018), p. 211.

[10] X.Y. Wu, Z.Y. Zhang, W.C. Qi, R.Y. Tian, S.M. Huang, and C.Y. Shi, Corrosion behavior of SMA490BW steel and welded joints for high-speed trains in atmospheric environments, *Materials*, 12(2019), No. 18, art. No. 3043.

[11] Q. Zhu, H. Yu, J.Q. Zhang, M. Li, and X.G. Hu, Experimental study on Tig welding properties of 6061 and 7003 aluminum alloys, [in] *Proceedings of the 2020 5th International Conference on Renewable Energy and Environmental Protection*, Shenzhen, 2020.

[12] T.H. Naing and P. Muangjunburee, Metallurgical and mechanical characterization of MIG welded repair joints for 6082-T6 aluminum alloy with ER 4043 and ER 5356, *Trans. Indian Inst. Met.*, 75(2022), No. 6, p. 1583.

[13] R.J. Griffiths, M.E.J. Perry, J.M. Sietins, *et al.* , A perspective on solid-state additive manufacturing of aluminum matrix composites using MELD, *J. Mater. Eng. Perform.*, 28(2019), No. 2, p. 648.

[14] W.D. Hartley, D. Garcia, J.K. Yoder, *et al*., Solid-state cladding on thin automotive sheet metals enabled by additive friction stir deposition, *J. Mater. Process. Technol.*, 291(2021), art. No. 117045.

[15] H.Z. Yu, M.E. Jones, G.W. Brady, *et al*., Non-beam-based metal additive manufacturing enabled by additive friction stir deposition, *Scripta Mater.*, 153(2018), p. 122.

[16] D. Garcia, W.D. Hartley, H.A. Rauch, *et al*., *In situ* investigation into temperature evolution and heat generation during additive friction stir deposition: A comparative study of Cu and Al–Mg–Si, *Addit. Manuf.*, 34(2020), art. No. 101386.

[17] Y.D. Li, B.B. Yang, M. Zhang, *et al*., The corrosion behavior and mechanical properties of 5083 Al–Mg alloy manufactured by additive friction stir deposition, *Corros. Sci.*, 213(2023), art. No. 110972.

[18] P. Agrawal, R.S. Haridas, S. Yadav, *et al*., Processing-structure-property correlation in additive friction stir deposited Ti–6Al–4V alloy from recycled metal chips, *Addit. Manuf.*, 47(2021), art. No. 102259.

[19] C.J.T. Mason, R.I. Rodriguez, D.Z. Avery, *et al*., Process-structure-property relations for as-deposited solid-state additively manufactured high-strength aluminum alloy, *Addit. Manuf.*, 40(2021), art. No. 101879.

[20] F. Khodabakhshi and A.P. Gerlich, Potentials and strategies of solid-state additive friction-stir manufacturing technology: A critical review, *J. Manuf. Processes*, 36(2018), p. 77.

[21] C.Y. Zeng, H. Ghadimi, H. Ding, *et al*., Microstructure evolution of Al6061 alloy made by additive friction stir deposition, *Materials*, 15(2022), No. 10, art. No. 3676.

[22] B.J. Phillips, C.J. Williamson, R.P. Kinser, J.B. Jordon, K.J. Doherty, and P.G. Allison, Microstructural and mechanical characterization of additive friction stir-deposition of aluminum alloy 5083 effect of lubrication on material anisotropy, *Materials*, 14(2021), No. 21, art. No. 6732.

[23] G.R. Merritt, M.B. Williams, P.G. Allison, J.B. Jordon, T.W. Rushing, and C.A. Cousin, Closed-loop temperature and force control of additive friction stir deposition, *J. Manuf. Mater. Process.*, 6(2022), No. 5, art. No. 92.

[24] K. Anderson-Wedge, D.Z. Avery, S.R. Daniewicz, *et al*., Characterization of the fatigue behavior of additive friction stir-deposition AA2219, *Int. J. Fatigue*, 142(2021), art. No. 105951.

[25] O.G. Rivera, P.G. Allison, L.N. Brewer, *et al*., Influence of texture and grain refinement on the mechanical behavior of AA2219 fabricated by high shear solid state material deposition, *Mater. Sci. Eng. A*, 724(2018), p. 547.

[26] Y.D. Li, M. Zhang, H. Wang, R.L. Lai, B.B. Yang, and Y.P. Li, Microstructure and mechanical properties of Al–Li alloy manufactured by additive friction stir deposition, *Mater. Sci. Eng. A*, 887(2023), art. No. 145753.

[27] W.S. Tang, X.Q. Yang, C.B. Tian, and C. Gu, Effect of rotation speed on microstructure and mechanical anisotropy of Al-5083 alloy builds fabricated by friction extrusion additive manufacturing, *Mater. Sci. Eng. A*, 860(2022), art. No. 144237.

[28] Z.K. Shen, M.T. Zhang, D.X. Li, *et al*., Microstructural characterization and mechanical properties of AlMg alloy fabricated by additive friction stir deposition, *Int. J. Adv. Manuf. Technol.*, 125(2023), No. 5-6, p. 2733.

[29] W.S. Tang, X.Q. Yang, C.B. Tian, and Y.S. Xu, Interfacial grain structure, texture and tensile behavior of multilayer deformation-based additively manufactured Al 6061 alloy, *Mater. Charact.*, 196(2023), art. No. 112646.

[30] F.C. Liu, P.S. Dong, A.S. Khan, *et al*., 3D printing of fine-grained aluminum alloys through extrusion-based additive manufacturing: Microstructure and property characterization, *J. Mater. Sci. Technol.*, 139(2023), p. 126.

[31] W.S. Tang, X.Q. Yang, and C.B. Tian, Influence of rotation speed on interfacial bonding mechanism and mechanical performance of aluminum 6061 fabricated by multilayer friction-based additive manufacturing, *Int. J. Adv. Manuf. Technol.*, 126(2023), No. 9-10, p. 4119.

[32] W. Gong, Y.D. Li, M. Zhang, *et al*., Influence of preheating temperature on the microstructure and mechanical properties of 6061/TA1 composite plates fabricated by AFSD, *Materials*, 16(2023), No. 17, art. No. 6018.

[33] J.K. Yoder, R.J. Griffiths, and H.Z. Yu, Deformation-based additive manufacturing of 7075 aluminum with wrought-like mechanical properties, *Mater. Des.*, 198(2021), art. No. 109288.

[34] V. Gopan, K. Leo Dev Wins, and A. Surendran, Innovative potential of additive friction stir deposition among current laser based metal additive manufacturing processes: A review, *CIRP J. Manuf. Sci. Technol.*, 32(2021), p. 228.

[35] S.S. Joshi, S.M. Patil, S. Mazumder, *et al*., Additive friction stir deposition of AZ31B magnesium alloy, *J. Magnesium Alloys*, 10(2022), No. 9, p. 2404.

[36] S. Sharma, K.V.M. Krishna, M. Radhakrishnan, *et al*., A pseudo thermo-mechanical model linking process parameters to microstructural evolution in multilayer additive friction stir deposition of magnesium alloy, *Mater. Des.*, 224(2022), art. No. 111412.

[37] J.L. Priedeman, B.J. Phillips, J.J. Lopez, *et al*., Microstructure development in additive friction stir-deposited Cu, *Metals*, 10(2020), No. 11, art. No. 1538.

[38] O. Rivera, P. Allison, J.B. Jordon, *et al*., Microstructures and mechanical behavior of Inconel 625 fabricated by solid-state additive manufacturing, *Mater. Sci. Eng. A*, 694(2017), p. 1.
[39] P. Agrawal, R.S. Haridas, S. Yadav, S. Thapliyal, A. Dhal, and R.S. Mishra, Additive friction stir deposition of SS316: Effect of process parameters on microstructure evolution, *Mater. Charact.*, 195(2023), art. No. 112470.
[40] R.J. Griffiths, D.T. Petersen, D. Garcia, and H.Z. Yu, Additive friction stir-enabled solid-state additive manufacturing for the repair of 7075 aluminum alloy, *Appl. Sci*., 9(2019), No. 17, p. 3486.
[41] D.Z. Avery, C.E. Cleek, B.J. Phillips, *et al*., Evaluation of microstructure and mechanical properties of Al–Zn–Mg–Cu alloy repaired via additive friction stir deposition, *J. Eng. Mater. Technol.*, 144(2022), No. 3, art. No. 031003.
[42] L.P. Martin, A. Luccitti, and M. Walluk, Repair of aluminum 6061 plate by additive friction stir deposition, *Int. J. Adv. Manuf. Technol.*, 118(2022), No. 3-4, p. 759
[43] Y.J. Li, W.Z. Zhang, and K. Marthinsen, Precipitation crystallography of plate-shaped $Al_6$(Mn,Fe) dispersoids in AA5182 alloy, *Acta Mater.*, 60(2012), No.17, p. 5963.
[44] Z.P. Que, Y. Wang, Z.Y. Fan, T. Hashimoto, and X.R. Zhou, Enhanced heterogeneous nucleation of $Al_6$(Fe,Mn) compound in Al alloys by interfacial segregation of Mn on $TiB_2$ particles surface, *Mater. Lett.*, 323(2022), p. art. No. 132570.
[45] F.J. Humphreys, Quantitative metallography by electron backscattered diffraction, *J. Microsc.*, 195(1999), p. 170.
[46] M.E.J. Perry, R.J. Griffiths, D. Garcia, J.M. Sietins, Y. Zhu, and H.Z. Yu, Morphological and microstructural investigation of the non-planar interface formed in solid-state metal additive manufacturing by additive friction stir deposition, *Addit. Manuf.*, 35(2020), art. No. 101293.
[47] R.J. Griffiths, D. Garcia, J. Song, *et al*., Solid-state additive manufacturing of aluminum and copper using additive friction stir deposition: Process-microstructure linkages, *Materialia*, 15(2021), p. 82.
[48] S. Beck, B.A. Rutherford, D.Z. Avery, *et al*., The effect of solutionizing and artificial aging on the microstructure and mechanical properties in solid-state additive manufacturing of precipitation hardened Al–Mg–Si alloy, *Mater. Sci. Eng. A*, 819(2021), art. No. 141351.
[49] B.J. Phillips, D.Z. Avery, T. Liu, *et al*., Microstructure-deformation relationship of additive friction stir-deposition Al–Mg–Si, *Materialia*, 7(2019), art. No. 100387.
[50] W.S. Tang, X.Q. Yang, C.B. Tian, and Y.S. Xu, Microstructural heterogeneity and bonding strength of planar interface formed in additive manufacturing of Al–Mg–Si alloy based on friction and extrusion, *Int. J. Miner. Metall. Mater.*, 29(2022), No. 9, p. 1755.
[51] H.S. Kim, Y. Estrin, and M.B. Bush, Plastic deformation behaviour of fine-grained materials, *Acta Mater.*, 48(2000), No.2, p. 493.
[52] C.X. Zhu, X.H. Tang, Y. He, F.G. Lu, and H.C. Cui, Effect of preheating on the defects and microstructure in NG-GMA welding of 5083 Al-alloy, *J. Mater. Process. Technol.*, 251(2018), p. 214.
[53] M. Jawad, M. Jahanzaib, M.A. Ali, *et al*., Revealing the microstructure and mechanical attributes of pre-heated conditions for gas tungsten arc welded AISI 1045 steel joints, *Int. J. Press. Vessels Pip.*, 192(2021), art. No. 104440.
[54] V.S. Gadakh and K. Adepu, Heat generation model for taper cylindrical pin profile in FSW, *J. Mater. Res. Technol.*, 2(2013), No.4, p. 370.
[55] A. Barbini, J. Carstensen, and J.F. dos Santos, Influence of a non-rotating shoulder on heat generation, microstructure and mechanical properties of dissimilar AA2024/AA7050 FSW joints, *J. Mater. Sci. Technol.*, 34(2018), No. 1, p. 119.
[56] M. Maalekian, E. Kozeschnik, H.P. Brantner, and H. Cerjak, Comparative analysis of heat generation in friction welding of steel bars, *Acta Mater.*, 56(2008), No.12, p. 2843.
[57] Z.K. Zhang, X.B. Li, Z.L. Zhao, C.M. Jiang, and H.X. Zhao, Process optimization and formation analysis of friction plug welding of 6082 aluminum alloy, *Metals*, 10(2020), No.11, art. No. 1454.
[58] S.D. Ji, X.C. Meng, R.F. Huang, L. Ma, and S.S. Gao, Microstructures and mechanical properties of 7N01-T4 aluminum alloy joints by active-passive filling friction stir repairing, *Mater. Sci. Eng. A*, 664(2016), p. 94.
[59] L.P. Martin, A. Luccitti, and M. Walluk, Evaluation of additive friction stir deposition for the repair of cast Al–1.4Si–1.1Cu–1.5Mg–2.1Zn, *J. Manuf. Sci. Eng.*, 144(2022), No. 6, art. No. 061006.
[60] Z.Y. Zhang, X.G. Sun, S.M. Huang, *et al*., Microstructure, mechanical properties and corrosion behavior of the aluminum alloy components repaired by cold spray with Al-based powders, *Metals*, 11(2021), No. 10, art. No. 1633.